Design of new-concept magnetomechanical devices by phase-field simulations

Jia-Mian Hu*

Department of Materials Science and Engineering, University of Wisconsin-Madison, Madison, WI, 53706

Abstract

Phase-field method enables simulating the spatiotemporal evolution of the coupled physical order parameters under externally applied fields in a wide range of materials and devices. Leveraging advanced numerical algorithms for solving the nonlinear partial differential equations and scalable parallelization techniques, phase-field method is becoming a powerful computational tool to model and design devices operating based on multiple coupled physical processes. This article will highlight examples of applying phase-field simulations to predict new mesoscale physical phenomena and design new-concept magnetomechanical devices by identifying the desirable combination of the composition, size, and geometry of monolithic materials as well as the device structure. A brief outlook of the opportunities and challenges for modeling and designing magnetomechanical devices with phase-field modeling is also provided.

*E-mail: jhu238@wisc.edu

Keywords: acoustic waves, modeling, magnetic, piezoelectric, photonic

Introduction

All magnetic devices operate by the control of spin (the spin angular momentum of electrons) or its continuum-scale quantity — magnetization (the density of magnetic moment per unit volume) — by externally applied fields. In the (quasi-)static limit, switching the magnetization (**M**) by an externally applied magnetic field, an electric current (via spin-transfer torque or spin-orbit torques[1]), or an electric field (via the magnetoelectric effect[2–8]) underpin the development of magnetoresistive random access memory (MRAM), magnetic-field sensors[9], and magnetic recording media[10]. Driving coupled ferromagnetic-ferroelastic domain (magneto-structural) switching by a magnetic field, as in ferromagnetic shape memory alloys[11,12], can be used for magnetic actuation. Driving magnetic phase transition (e.g., paramagnetic to ferromagnetic) near the transition temperature using a magnetic field, as in magnetocaloric materials[13], can be used for magnetic refrigeration. Dynamical excitation of spin, i.e., spin wave (or its quantum, magnon), has many fundamentally intriguing and technologically important physical features. For example, the strong quantum-mechanical exchange interaction among neighboring spins gives rise to highly nonlinear magnon frequency dispersion[14]. The intrinsic nonlinearity of the Landau-Lifshitz-Gilbert (LLG) equation — the equation of motion for spin — results in nonlinear magnon-magnon interaction (e.g., frequency doubling and shifting)[15]. Unlike electron transport, magnon transport can occur in electronically insulating materials with up to micrometer-scale decay length[16,17]. Furthermore, magnons can be hybridized with other magnon modes[18] and other quasiparticles such as acoustic phonons, photons, and superconducting qubits[19–23], allowing coherent quantum state transfer among different physical systems. Therefore, magnons have found an extremely broad range of potential applications, ranging from wave-based computing[24,25] to higher-frequency electromagnetic (EM) radiation[26–29] and to microwave-optical quantum transduction[30] and other quantum operations[31,32]. **Figure 1** illustrates a few types of magnetic order manipulation.

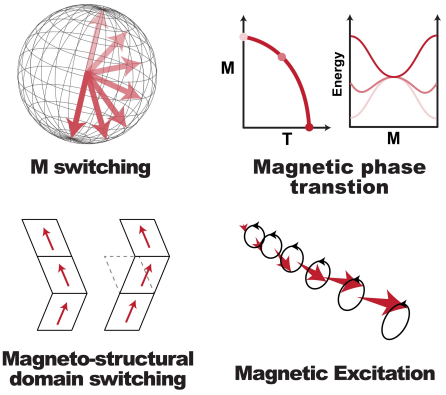

Figure 1. Different types of magnetic order manipulation.

Phase-field method allows for simulating the coupled evolution of magnetization with other physical order parameters, such as strain, electrical polarization, and EM waves, in material and devices of arbitrary geometry under complex magnetic, electric, mechanical, and EM boundary conditions. Phase-field method draws its strength from the integration of micromagnetic, elastostatic/elastodynamic, and EM modeling methods to enable the simulation of a comprehensive set of physical phenomena that cannot be (accurately) simulated with individual modeling methods. For example, compared to conventional micromagnetic modeling, phase-field models that couple micromagnetics with elastostatics (i.e., $\nabla \cdot \boldsymbol{\sigma}=0$, where $\boldsymbol{\sigma}$ is mechanical stress)[33,34] or elastodynamics ($\nabla \cdot \boldsymbol{\sigma} = \rho \ddot{\mathbf{u}}$ if omitting the elastic damping, where ρ is the mass density and $\mathbf{u}$ is the mechanical displacement)[35–37] are particularly suited for simulating the equilibrium magnetization patterns and their evolution under external fields in magnetic materials exhibiting strong magnetoelastic coupling. It is noteworthy that any computational models that employ a continuum-scale order parameter and its gradient in the thermodynamic potential (energy density) function may be called a phase-field model[38]. In this regard, a micromagnetic-elastodynamic phase-field model is equivalent to other multiphysics

models that incorporate coupled micromagnetics and elastodynamics[39,40]. If incorporating a Landau-type energy term of the magnitude of the magnetization **M** into the thermodynamic potential, phase-field modeling can be used to model the magnetization pattern evolution during the magnetic or magneto-structural phase transition in ferromagnetic shape memory alloys[41–43]. If incorporating the coupling to electrical polarization via intrinsic magnetoelectric effect or strain, phase-field modeling would allow modeling the electric-field control of magnetic domains and their coupled evolution to polarization and strain domains in multiferroic compounds (e.g., $BiFeO_3$[44] and $YMnO_3$[45]) and composite multiferroic heterostructures and nanostructures[46–48]. More recently, dynamical phase-field models that incorporate fully coupled dynamics of magnetization, strain, and EM waves have been developed[35–37,49], which enables the simulation of a wide variety of magnetic phenomena driven by external stimuli that are faster than the eigenmode oscillation. This article is focused on the application of phase-field simulations to design two types of new-concept magnetomechanical devices, which operate based on (quasi)static or dynamical magnetoelastic coupling, respectively. An outlook on the opportunities and challenges of using phase-field method to design magnetomechanical devices based on other types of magnetic materials and systems is also provided.

Magnetoelastic coupling in the (quasi)static regime

Magnetoelastic coupling constants B_i (i=1,2,…), with a unit of J/m^3, are the coefficients in the first-order derivative of the magnetocrystalline anisotropy energy density with respect to strain[50–52]. These constants thus represent the efficiency of converting elastic energy to magnetic energy in the (quasi)static limit. First-principles density functional theory calculations can be used to predict the magnetocrystalline anisotropy as a function of strain, through which B_i can be evaluated[53,54]. The magnetoelastic energy density of a ferromagnet with a cubic paramagnetic phase at above the Curie temperature can be written as[50–52],

$$f^{\mathrm{mel}} = B_1\left(\varepsilon_{xx}m_x^2 + \varepsilon_{yy}m_y^2 + \varepsilon_{zz}m_y^2\right) + 2B_2\left(m_x m_y \varepsilon_{xy} + m_y m_z \varepsilon_{yz} + m_x m_z \varepsilon_{xz}\right) + \cdots (1)$$

Here the B_1=-1.5λ_{100}(c_{11}-c_{12}) and B_2=-3$\lambda_{111}c_{44}$; λ_{100} and λ_{111} are saturation magnetostriction constants along the <100> and <111> axes, respectively; $m_i = M_i/M_s$ (i=x,y,z) are the normalized magnetization along the Cartesian axes and M_s is the saturation magnetization; ε_{ij} (i,j=x,y,z) are the total strain that need to be determined based on the mechanical boundary condition. Since f^{mel} is part of the total magnetic free energy[3], applying strain to a magnetic material can shift the global energy minima and hence rotate the magnetic easy axis. Thermodynamic analyses predict that strain-mediated voltage-driven magnetic easy axis rotation is up to 90°, and can be abrupt or continuous, electrically volatile or nonvolatile in strained single-domain magnetic thin films[55,56]. Strain-induced up to 90° magnetization switching in multi-domain magnetic thin films and nanostructures was later demonstrated by phase-field simulations[34,47,57] and the nanoscale vector map of local magnetization obtained from x-ray magnetic circular dichroism—photoemission electron microscopy imaging[58,59]. The f^{mel} of an antiferromagnetic (AFM) material can be evaluated by extending **Equation (1)** to all the magnetic sublattices[36,60–62]. Experimentally, strain-induced reorientation of the Néel vector in AFM thin films[63,64] and strain-modulation of AFM phase transition[65] have been achieved.

Magnon-phonon coupling (dynamical magnetoelastic coupling)

The magnon-phonon coupling strength g_{mp}, with a unit of Hz, is defined as the half of frequency gap in the dispersion relation of magnon polaron, similarly to other two-level systems[66]. The magnon

polaron is the quantum of the so-called magnetoelastic wave[67] and forms through the hybridization of magnon and acoustic phonon when their frequency (f) and wavenumber (k) are similar, as indicated in **Figure 2**(a). In a magnetoelastic wave, the energy of the wave is transferred back-and-forth between magnon and phonon subsystems with almost 100% efficiency[37,68]. The g_{mp} represents the rate of such dynamical energy transduction. Larger magnetoelastic coupling constants B_i will result in a larger g_{mp}. When g_{mp} is larger than the energy dissipation rates (unit: Hz) of individual magnon modes (κ_{m}) and phonon modes (κ_{p}), the magnon-phonon coupling enters the strong coupling regime. To preserve the phase of dynamic excitation (i.e., coherence) during the energy transduction, as required in many quantum operations, the cooperativity $C = g_{\mathrm{mp}}^2/(\kappa_{\mathrm{m}}\kappa_{\mathrm{p}})$ typically needs to be greater than one [66]. Analytical solution of the magnon polaron dispersion relation and hence the g_{mp} can be obtained by linearizing the coupled LLG and elastodynamic equations under zero magnetic and elastic damping[37,69], as shown in Figure 2(b-c).

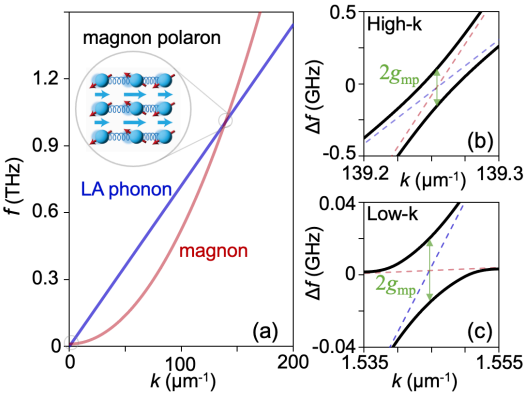

Figure 2. (a) Dispersion relation of the longitudinal acoustic (LA) phonon and exchange magnons in (001) $Y_3Fe_5O_{12}$ (YIG) bulk crystal. (b-c) high-k and low-k magnon polaron dispersion relation. A bias magnetic field (H_x^b, H_y^b, H_z^b)= (0.2513 T, 0, 0.376 T) is applied. The wavevector k is along z. These dispersion relations are calculated analytically using the materials parameters of YIG and formulae provided in ref. 37.

The dynamical phase-field simulations suggest that the formation of magnon polarons simultaneously requires closely matched frequency and wavenumber between magnons and acoustic phonons, sufficiently long magnon-phonon interaction time, and sufficiently low magnetic and elastic damping[37]. Thus far, direct experimental observation of magnon polarons have been limited to a few magnetic systems[68,70–74]. Nevertheless, magnons and acoustic phonons are always coupled to some extent (a.k.a., dynamical magnetoelastic coupling[60]). This is because both the magnetoelastic coupling coefficient (which is related to the excitation of magnons by acoustic phonons) and the magnetostrictive coefficient (which is related to the generation of acoustic phonons by magnons), as a four-rank tensor, are non-zero in any magnetic materials. If a magnon polaron does not form ($g_{\mathrm{mp}}\approx 0$), the strength of the magnon-phonon coupling can be quantified by either the energy transfer efficiency between the elastic wave and the spin wave[75] or the magnetoelastic Hamiltonian[76,77].

Design of voltage-driven MRAM based on strain-mediated magnetic switching

Phase-field models incorporating coupled micromagnetics and elastostatics[33,34] are suitable for simulating equilibrium magnetization distribution and magnetization dynamics under static or low-frequency (i.e., substantially slower than magnetization dynamics) strains. This section presents examples of applying such micromagnetic-elastostatic phase-field models to design strain-mediated voltage-driven MRAM, the energy efficiency and the overall performance of which can potentially eclipse all the competing technologies[6]. Specifically, phase-field simulations can be used to identify material composition, device size and geometry that lead to the desirable device attributes such as high storage capacity, low energy dissipation, and high write speed [78].

As mentioned earlier, strain can rotate the magnetic easy axis by up to 90° via the (quasi)static magnetoelastic coupling. In a single-domain nanomagnet, this means that a magnetization vector initially aligning along $+x$ has an equal probability of being switched to $+y$ or $-y$. In an MRAM, such non-deterministic 90° switching can still result in a substantial change in the electrical resistance of the giant magnetoresistive element or magnetic tunnel junction[79]. By applying voltage to an adjacent piezoelectric layer, strain-mediated voltage-driven MRAM with ultralow write energy has been computationally designed[78] (see **Figure 3**(a)) and experimentally demonstrated[80]. Furthermore, as illustrated in Figure 3(b), one can first apply strain to trigger a >90° transient magnetization switching and then turn off the strain to let the magnetization relax to its neighboring energy minimum, thereby achieving a 180° perpendicular magnetization reversal[81,82], with promising applications in low-power perpendicular MRAM. Such a scheme of dynamical strain control has later been extended to realize a strain-mediated 360° magnetic domain-wall motion in a ring-shaped nanomagnet[83], with applications to ring-based low-power MRAM[84] and energy-efficient nanoscale magnetic motors[85]. As shown in Figure 3(c), multiple electrodes are used to alternatively generate uniaxial piezostrains along different axes in the xy plane. The resulting 360° domain-wall motion can be seen from the spatial trajectory of the average in-plane magnetization $\langle m_x \rangle$ and $\langle m_y \rangle$ of the nanoring and the local magnetization vector distribution. More recently, phase-field simulations have predicted that piezostrains can enable a nonvolatile and repeatable switching between an isolated magnetic skyrmion and a quasi-single magnetic domain (i.e., with tilted spins along the edges) in patterned nanodisks[86,87], as shown in Figure 3(d). Such a phenomenon, with applications to voltage-driven skyrmion-based MRAM, has later been observed experimentally in similar magnetoelectric heterostructures[88,89].

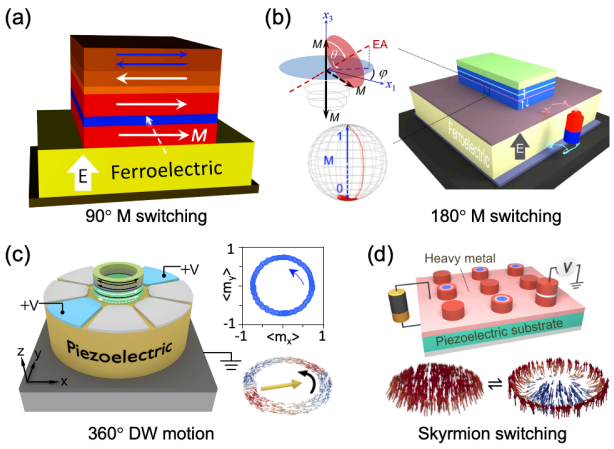

Figure 3. Design of voltage-driven MRAM based on strain-mediated (a) 90° in-plane magnetization switching (Reproduced with permission from ref. 78). (b) 180° perpendicular magnetization switching (Adapted with permission from ref. 81. Copyright 2015 American Chemical Society); (c) 360° magnetic domain-wall (DW) motion (Adapted with permission from ref. 83. Copyright 2016 American Chemical Society); and (d) skyrmion switching (Adapted with permission from ref. 86).

Design of dynamically tunable, narrowband THz emitter based on magnon-phonon coupling

The frequency window of an optically induced acoustic pulse (acoustic phonons) typically covers from tens to hundreds of gigahertz[90] but can reach up to several terahertz (THz)[91]. When injecting such photoinduced acoustic pulse into a magnetic material (see a recent review[92]), magnons of the same frequencies as the driving acoustic phonons can be excited via the magnetoelastic coupling. To simulate such coupled phonon-magnon dynamics, coupled LLG-elastodynamic model[39,40] is needed. Moreover, high-frequency magnetization oscillation may produce strong EM wave whose magnetic-field component would in turn modulate the magnetization dynamics. When the amplitude of the emitted EM wave is large, such backaction from EM radiation can be significant. Incorporating such backaction requires a coupled elastodynamic-LLG-Maxwell model. Furthermore, the emitted EM wave can induce large eddy currents (plasmons) in the metallic components of magnetic devices. In

this case, the dynamics of eddy current needs to be self-consistently integrated in the numerical solution of the coupled LLG-Maxwell equations[93,94]. This section presents the application of the recently developed dynamical phase-field model[35–37,49], which incorporates coupled phonon-magnon-photon-plasmon dynamics by solving the exact forms of the coupled elastodynamic, LLG, Maxwell, and eddy current dynamics equations, to design new-concept THz emitters[35,36,95]. These THz emitters have distinct performances but all operate based on the excitation of THz magnons by a femtosecond(fs)-laser-induced acoustic pulse. Details of the proposed device structures are described in several patents (US11112355B2, US11199447B1, US11817242B2). These emitters provide the much-needed narrowband THz pulse whose peak frequency can be tuned by varying the applied bias magnetic field. These features, which complement the previously existing fs-laser-driven THz emitters that are broadband and difficult to tune dynamically, enable exciting potential applications in narrowband spectroscopy, high-spectral-resolution imaging, and high-data-rate wireless communication.

These new-concept THz emitters are comprised of multilayer magnetic heterostructures in different forms yet all involve a magnetic film adjacent to a paramagnetic metal film that permits the spin-to-charge current conversion via the inverse Spin Hall effect[96]. The emitter THz wave is largely generated by the THz a.c. charge current in the paramagnetic metal layer. The a.c. charge current is converted from the a.c. spin current[97], which arises from the precession of magnetization at the magnet/paramagnetic-metal interface via spin pumping. The acoustically excited magnons in the magnetic layer, due to their symmetric spatial mode profiles, produce negligible EM wave emission themselves[98]. The dynamical phase-field simulation results have suggested that the eddy currents in the metal layer significantly reduce the overall THz emission[35,36,95]. Furthermore, the simulations also indicate the necessity of considering the spin-pumping-induced magnetic damping[99].

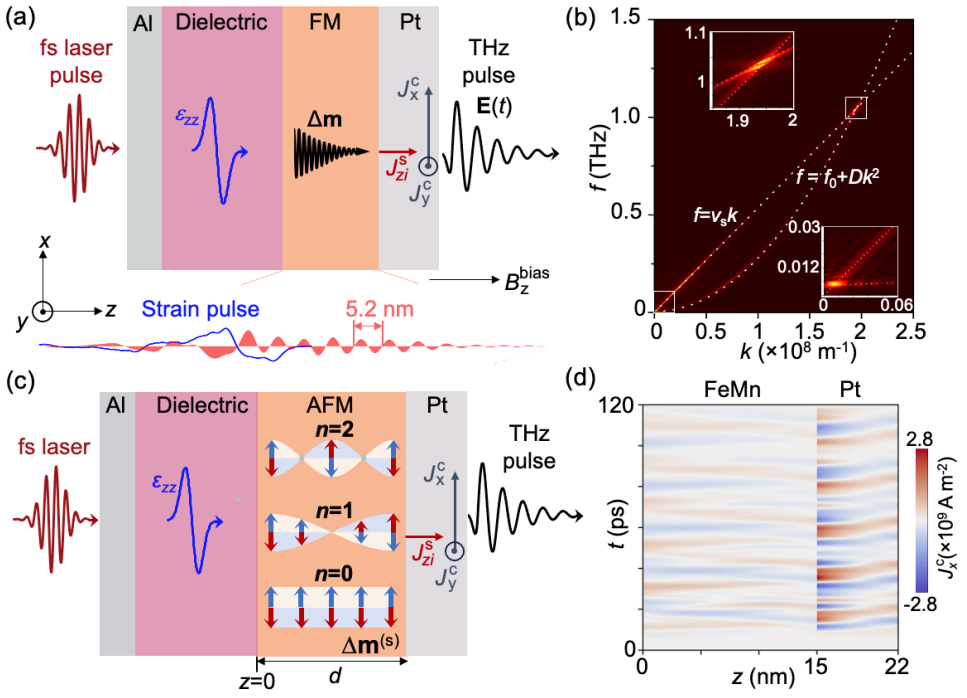

Figure 4. (a) Schematic of the THz emitter that involves the use of a thick ferromagnetic (FM) film. $\varepsilon_{zz}(z,t)$ is the strain pulse generated by irradiating the aluminum (Al) layer with a fs laser pulse. Other metallic photoacoustic transducers can also be used. The plot in the bottom panel shows the representative spatial profiles of the elastic wave and spin wave at 10 ps after the strain pulse propagates into the FM film, for which a 900-nm-thick (001) Fe film is used as an example. (b) Dispersion relation of the

acoustically excited magnons in the (001) Fe film, obtained by dynamical phase-field simulations (colored background) and analytical calculation (dotted line). (c) Schematic of the THz emitter that involves the use of a thin antiferromagnetic (AFM) film. The vectors, sketched along *z*, do not indicate the actual direction of the spins in the magnetic sublattices. The spin current J_{zi}^{s} (i=x,y,z) is a second-rank tensor, where the first subscript '*z*' indicates the direction of the current flow yet the second subscript '*i*' indicates the direction of spin polarization. (d) Spatiotemporal evolution of the charge current density component J_c^x in the FeMn/Pt metallic bilayer. t=0 ps is the moment strain pulse propagates into the AFM FeMn film from its bottom surface (z=0). (a-b) Adapted with permission from ref. 35. Copyright 2021 American Chemical Society; (c-d) adapted with permission from ref. 36.

Quasi-monochromatic THz emitter based on acoustic excitation of propagating THz magnons. **Figure 4**(a) shows one presentation of such THz emitter. The photoacoustic transduction process can be simulated by combining the two-temperature model (for incorporating electron-phonon coupling), heat transport, and elastodynamics[35]. A thick FM film is used to allow the propagation of exchange-coupling-dominated THz magnons along the *z* direction. Such THz exchange magnons travel twice as fast as the strain pulse, as illustrated in the bottom panel of Figure 4(a). The excitation mechanism is more clearly explained by the numerically calculated magnon frequency dispersion relation, which is obtained by Fourier transform of the $\Delta\mathbf{m}(z,t)$ in the magnetic layer. As shown in Figure 4(b), some of the acoustically excited magnons have a linear frequency (f) – wavenumber (k) relationship with a group velocity ($\partial f/\partial k$) the same as the longitudinal speed of sound v_s. These magnons propagate along with the acoustic phonons. The simulated f–k relationship can be well described using $f=v_s k$. Other acoustically excited magnons have a parabolic f–k dispersion relation, which agrees well with analytical prediction via $f=f_0+Dk^2$. Here f_0 is the ferromagnetic resonance frequency and the coefficient $D=(4\pi A_{ex}\gamma)/(\mu_0 M_s)$; A_{ex} is exchange coupling coefficient; γ is gyromagnetic ratio; μ_0 is vacuum permeability; M_s is saturation magnetization. At the two crossing points, where f and k of the magnon modes match those of the acoustic phonons, both the spectral amplitude and the magnetization amplitude of those magnon modes are significantly enhanced due to the resonant magnon-phonon interaction, as shown by the two insets in Figure 4(b). However, there is no avoided crossing (formation of magnon polarons) in this case (c.f., Figure 2) due to the relatively large magnetic damping and/or the insufficient magnon-phonon interaction time. Furthermore, the spin current resulting from the magnons at the high-k crossing point (~1.04 THz) is much larger than those at the low-k crossing point (~4.73 GHz). Ultimately, the emitted THz wave becomes quasi-monochromatic with a dominant component at 1.04 THz. Furthermore, the frequency at the high-k crossing point (f^*) can be analytically evaluated as $f^* = \left(v_s^2 + v_s\sqrt{v_s^2 - 4Df_0}\right)/(2D)$, where the f_0 can be tuned by varying the bias magnetic field. Moreover, this equation indicates the f^* has a lower bound of $v_s^2/(2D)$ at $f_0 = v_s^2/(4D)$ and an upper bound of v_s^2/D at $f_0 \approx 0$. Thus, one can apply magnetic field to dynamically tune the frequency of the dominant magnon mode and the resulting THz emission by up to 50%, e.g., from about 1.04 THz to 0.52 THz.

Multi-mode narrowband THz emitter based on acoustic excitation of standing THz magnons. When magnetic layer is relatively thin (e.g., a few to tens of nanometers) and interfaced with non-magnetic material, standing exchange magnons with harmonic angular wavenumbers $k=n\pi/d$ (n=0, 1,2,3…; d is the magnetic layer thickness) can be excited. Experimentally, optically induced spin transfer torque[100] or spin-orbit torque[101] have been used to excite such harmonic magnon modes in FM thin films (Fe[100] and $Ni_{81}Fe_{19}$[101]) with frequency up to 0.6 THz. Recent theoretical and computational works have suggested that photoinduced acoustic pulse can also excite these harmonic standing exchange magnons in FM thin films[102,103]. This strategy has later been extended to AFM multilayer (see one representative design in Figure 4(c)). Using a γ-$Fe_{50}Mn_{50}$ (FeMn) thin film-based multilayer as an example, magnetic-field-free excitation of THz AFM standing exchange magnon modes by acoustic pulse was

demonstrated using dynamical phase-field simulations[36]. The simulation results show that the two magnetic sublattices of FeMn can constructively pump spin current into the Pt thin film, leading to a higher THz output power than that from FM multilayer. The a.c. charge current in the Pt is contributed by both the iSHE charge current and the eddy current yet the charge current in the FeMn is solely contributed by eddy current. The spatiotemporal evolution of the charge current density component J_c^x in the FeMn/Pt bilayer is shown in Figure 4(d).

High-Q THz emitter and optoelectronic transducer based on hybrid magnon-phonon cavity. In the designs shown above (Figure 4(a) and 4(c)), the acoustic pulse stays in the magnetic layer for a relatively short period (about $2d/v_s$, which is 4 ps if assuming d=10 nm and v_s=5000 m/s). **Figure 5** shows a different device design based on a freestanding metal/magnetic-insulator/dielectric multilayer where multiple standing acoustic phonon modes would form after the injection of a single-cycle photoinduced acoustic pulse[95]. Thus, the freestanding multilayer works as a cavity for both the magnons and acoustic phonons, thereby enabling a more efficient harvesting of the acoustic energy for magnon excitation. Moreover, if the frequencies (ideally, both frequency and wavenumber) of the standing acoustic phonon modes match the standing exchange magnon modes, magnon modes with large magnetization amplitude can be excited through extended, resonant magnon-phonon interaction[104]. Based on dynamical phase-field simulations for both a freestanding and a substrate-supported multilayer, it has been found that the freestanding multilayer enables (i) an over ten times larger magnetization amplitude for the excited magnons; and (ii) significant enhancement in both the amplitude and duration of the free-space THz emission. Overall, the freestanding multilayer allows converting a single-cycle fs laser pulse into a multi-cycle, ns-long THz pulse (and a ns-long THz charge current pulse confined in the metal film) with large amplitude and high quality factor (Q), promising exciting applications not only as the THz emitter but also a THz optoelectronic transducer.

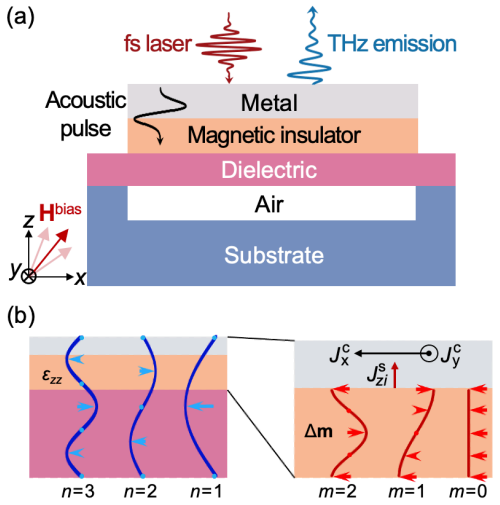

Figure 5. (a) Schematic of the freestanding multilayer on a substrate patterned with air cavity at its surface. (b) Illustration of the standing longitudinal acoustic phonons ε_{zz} with modes of n across the multilayer, and the standing exchange magnons $\Delta\mathbf{m}$ with modes of m in the magnetic insulator film. Varying the bias magnetic field $\mathbf{H}^{bias}$ enables dynamically tuning the frequencies of the m=0 magnon mode (ferromagnetic resonance) and thereby higher-order magnons. Taken from ref. 95.

Outlook

An overview of applying phase-field model to design strain-mediated voltage-driven MRAM and applying dynamical phase-field model to design THz magnonic devices was provided. There is still plenty of room for further development of phase-field models in concert with experimental efforts to understand and predict strain manipulation of magnetic order and guide the device design. For example, it would be intriguing to develop a phase-field model for simulating the mesoscale pattern formation and evolution during magneto-structural phase transition and strain-mediated control of magnetism in (1) freestanding magnetic membrane[105–107] which could sustain extremely large strain well beyond the limit of bulk crystal and substrate-clamped thin films, and (2) atomically thin van der

Waals magnets which display exotic phenomena such as strong exchange magnetostriction (i.e., strain modulation of direct spin-spin exchange interaction[108]). These mechanically flexible magnets not only provide a new material platform for studying the fundamental interplay among magnetism, geometry, topology, but also offer new potential applications in nano/macro-scale magnetic soft robots, biomedical engineering, and interactive electronics, as discussed in recent perspective articles[109,110] and a book[111]. It would also be beneficial to further develop the dynamical phase-field model to guide the design of hybrid magnonic devices for quantum operation (notably those based on tripartite entanglement among phonons, magnons, and photons[22,112,113]) towards quantum computing and long-distance quantum communication[114,115]. The computational time of phase-field simulations often increases significantly in modeling practical devices, due to the increased system size, the complexity of boundary conditions, and the nonlinearity of the governing equations. It would therefore be another interesting direction and may eventually become necessary to integrate machine learning methods for accelerating the phase-field simulations[116–120]. The ability to simulate practically sized materials/devices will further enhance the predictive power of phase-field modeling and facilitate the computation-enabled discovery of new mesoscale magnetic phenomena.

Conflict of Interests Statement

The corresponding author states that there is no conflict of interest.

References

1. A. Brataas, A. D. Kent, H. Ohno, *Nat Mater*. **11**, 372 (2012).
2. J.-M. Hu, T. Nan, N. X. Sun, L.-Q. Chen, *MRS Bull*. **40**, 728–735 (2015).
3. J.-M. Hu, L.-Q. Chen, C.-W. Nan, *Adv. Mater*. **28**, 15–39 (2016).
4. J.-M. Hu, C.-G. Duan, C.-W. Nan, L.-Q. Chen, *NPJ Comput Mater*. **3**, 18 (2017).
5. G. P. Carman, N. Sun, *MRS Bull*. **43**, 822–828 (2018).
6. J.-M. Hu, C.-W. Nan, *APL Mater*. **7**, 80905 (2019).
7. W. Eerenstein, N. D. Mathur, J. F. Scott, *Nature*. **442**, 759 (2006).
8. N. A. Spaldin, R. Ramesh, *Nat Mater*. **18**, 203–212 (2019).
9. D. Viehland, M. Wuttig, J. McCord, E. Quandt, *MRS Bull*. **43**, 834–840 (2018).
10. K. Hono, Y. K. Takahashi, G. Ju, J.-U. Thiele, A. Ajan, X. Yang, R. Ruiz, L. Wan, *MRS Bull*. **43**, 93–99 (2018).
11. T. Kakeshita, K. Ullakko, *MRS Bull*. **27**, 105–109 (2002).
12. R. C. O'Handley, S. J. Murray, M. Marioni, H. Nembach, S. M. Allen, *J Appl Phys*. **87**, 4712–4717 (2000).
13. X. Moya, S. Kar-Narayan, N. D. Mathur, *Nat Mater*. **13**, 439–450 (2014).
14. P. Pirro, V. I. Vasyuchka, A. A. Serga, B. Hillebrands, *Nat Rev Mater*. **6**, 1114–1135 (2021).
15. A. G. Gurevich, G. A. Melkov, *Magnetization Oscillations and Waves* (CRC Press, 2020).
16. L. J. Cornelissen, J. Liu, R. A. Duine, J. Ben Youssef, B. J. van Wees, *Nat Phys*. **11**, 1022–1026 (2015).
17. R. Lebrun, A. Ross, S. A. Bender, A. Qaiumzadeh, L. Baldrati, J. Cramer, A. Brataas, R. A. Duine, M. Kläui, *Nature*. **561**, 222–225 (2018).
18. Y. Li, W. Cao, V. P. Amin, Z. Zhang, J. Gibbons, J. Sklenar, J. Pearson, P. M. Haney, M. D. Stiles, W. E. Bailey, V. Novosad, A. Hoffmann, W. Zhang, *Phys Rev Lett*. **124**, 117202 (2020).
19. Y. Li, C. Zhao, W. Zhang, A. Hoffmann, V. Novosad, *APL Mater*. **9**, 60902 (2021).
20. X. Zhang, C.-L. Zou, L. Jiang, H. X. Tang, *Phys Rev Lett*. **113**, 156401 (2014).
21. Y. Li, T. Polakovic, Y.-L. Wang, J. Xu, S. Lendinez, Z. Zhang, J. Ding, T. Khaire, H. Saglam, R. Divan, J. Pearson, W.-K. Kwok, Z. Xiao, V. Novosad, A. Hoffmann, W. Zhang, *Phys Rev Lett*. **123**, 107701 (2019).
22. X. Zhang, C.-L. Zou, L. Jiang, H. X. Tang, *Sci Adv*. **2**, e1501286 (2016).

23. Y. Tabuchi, S. Ishino, A. Noguchi, T. Ishikawa, R. Yamazaki, K. Usami, Y. Nakamura, *Science (1979)*. **349**, 405–408 (2015).

24. A. V Chumak et al., *IEEE Trans Magn*. **58**, 1–72 (2022).

25. D. D. Yaremkevich, A. V Scherbakov, L. De Clerk, S. M. Kukhtaruk, A. Nadzeyka, R. Campion, A. W. Rushforth, S. Savel'ev, A. G. Balanov, M. Bayer, *Nat Commun*. **14**, 8296 (2023).

26. Z. Yao, Y. E. Wang, S. Keller, G. P. Carman, *IEEE Trans Antennas Propag*. **63**, 3335–3344 (2015).

27. M. Zaeimbashi, M. Nasrollahpour, A. Khalifa, A. Romano, X. Liang, H. Chen, N. Sun, A. Matyushov, H. Lin, C. Dong, Z. Xu, A. Mittal, I. Martos-Repath, G. Jha, N. Mirchandani, D. Das, M. Onabajo, A. Shrivastava, S. Cash, N. X. Sun, *Nat Commun*. **12**, 3141 (2021).

28. C. Bull, S. M. Hewett, R. Ji, C.-H. Lin, T. Thomson, D. M. Graham, P. W. Nutter, *APL Mater*. **9**, 090701 (2021).

29. Y. Ji, C. Zhang, T. Nan, *Phys Rev Appl*. **18**, 64050 (2022).

30. R. Hisatomi, A. Osada, Y. Tabuchi, T. Ishikawa, A. Noguchi, R. Yamazaki, K. Usami, Y. Nakamura, *Phys Rev B*. **93**, 174427 (2016).

31. D. D. Awschalom, C. R. Du, R. He, F. J. Heremans, A. Hoffmann, J. Hou, H. Kurebayashi, Y. Li, L. Liu, V. Novosad, J. Sklenar, S. E. Sullivan, D. Sun, H. Tang, V. Tyberkevych, C. Trevillian, A. W. Tsen, L. R. Weiss, W. Zhang, X. Zhang, L. Zhao, C. W. Zollitsch, *IEEE Trans. Quantum Eng*. **2**, 1–36 (2021).

32. H. Y. Yuan, Y. Cao, A. Kamra, R. A. Duine, P. Yan, *Phys Rep*. **965**, 1–74 (2022).

33. J. X. Zhang, L. Q. Chen, *Acta Mater*. **53**, 2845–2855 (2005).

34. J.-M. Hu, G. Sheng, J. X. Zhang, C. W. Nan, L. Q. Chen, *Appl Phys Lett*. **98**, 112505 (2011).

35. S. Zhuang, P. B. Meisenheimer, J. Heron, J.-M. Hu, *ACS Appl Mater Interfaces*. **13**, 48997–49006 (2021).

36. S. Zhuang, J. M. Hu, *NPJ Comput Mater*. **8**, 167 (2022).

37. S. Zhuang, J.-M. Hu, *J Phys D Appl Phys*. **56**, 54004 (2023).

38. L.-Q. Chen, Y. Zhao, *Prog Mater Sci*. **124**, 100868 (2022).

39. C.-Y. Liang, S. M. Keller, A. E. Sepulveda, A. Bur, W.-Y. Sun, K. Wetzlar, G. P. Carman, *Nanotechnology*. **25**, 435701 (2014).

40. A. V Azovtsev, N. A. Pertsev, *Appl Phys Lett*. **111**, 222403 (2017).

41. J. X. Zhang, L. Q. Chen, *Philos Mag Lett*. **85**, 533–541 (2005).

42. H. B. Huang, X. Q. Ma, J. J. Wang, Z. H. Liu, W. Q. He, L. Q. Chen, *Acta Mater*. **83**, 333–340 (2015).

43. D. Ohmer, M. Yi, O. Gutfleisch, B.-X. Xu, *Int J Solids Struct*. **238**, 111365 (2022).

44. F. Xue, T. Yang, L.-Q. Chen, *Phys Rev B*. **103**, 64202 (2021).

45. F. Xue, X. Wang, Y. Shi, S.-W. Cheong, L.-Q. Chen, *Phys Rev B*. **96**, 104109 (2017).

46. J. X. Zhang, Y. L. Li, D. G. Schlom, L. Q. Chen, F. Zavaliche, R. Ramesh, Q. X. Jia, *Appl Phys Lett*. **90**, 052909 (2007).

47. J.-M. Hu, T. N. Yang, L. Q. Chen, C. W. Nan, *J Appl Phys*. **113**, 194301 (2013).

48. T. N. Yang, J.-M. Hu, C. W. Nan, L. Q. Chen, *Appl Phys Lett*. **104**, 202402 (2014).

49. S. Zhuang, C. Zhong, L. Jiang, X. Zhang, J.-M. Hu, Preprint, available via https://doi.org/10.21203/rs.3.rs-3603404/v1 (2023).

50. C. Kittel, *Rev Mod Phys*. **21**, 541–583 (1949).

51. E W Lee, *Rep. Prog. Phys*. **18**, 184 (1955).

52. D Sander, *Rep. Prog. Phys*. **62**, 809 (1999).

53. Y. Zhang, H. Wang, R. Wu, *Phys Rev B*. **86**, 224410 (2012).

54. H. L. Zhuang, P. R. C. Kent, R. G. Hennig, *Phys Rev B*. **93**, 134407 (2016).

55. N. A. Pertsev, *Phys Rev B*. **78**, 212102 (2008).

56. J.-M. Hu, C. W. Nan, *Phys Rev B*. **80**, 224416 (2009).

57. J.-M. Hu, T. N. Yang, L. Q. Chen, C. W. Nan, *J Appl Phys*. **114**, 164303 (2013).

58. M. Ghidini, R. Mansell, F. Maccherozzi, X. Moya, L. C. Phillips, W. Yan, D. Pesquera, C. H. W. Barnes, R. P. Cowburn, J.-M. Hu, S. S. Dhesi, N. D. Mathur, *Nat Mater*. **18**, 840–845 (2019).

59. M. Ghidini, F. Maccherozzi, S. S. Dhesi, N. D. Mathur, *Adv Electron Mater*. **8**, 2200162 (2022).

60. F. Morgenthaler, *IEEE Trans Magn*. **8**, 130–151 (1972).

61. A. Barra, J. Domann, K. W. Kim, G. Carman, *Phys Rev Appl*. **9**, 34017 (2018).

62. P. A. Popov, A. R. Safin, A. Kirilyuk, S. A. Nikitov, I. Lisenkov, V. Tyberkevich, A. Slavin, *Phys Rev Appl*. **13**, 44080 (2020).

63. A. Kozioł-Rachwał, M. Ślęzak, M. Zając, P. Dróżdż, W. Janus, M. Szpytma, H. Nayyef, T. Ślęzak, *APL Mater*. **8**, 061107 (2020).

64. P. Shirazi, M. K. Panduranga, T. Lee, A. Barra, V. Estrada, D. L. Tran, A. E. Sepulveda, G. P. Carman, *Appl Phys Lett*. **120**, 202405 (2022).

65. W. P. Wolf, C. H. A. Huan, *J Appl Phys*. **63**, 3904–3909 (1988).

66. Y. Li, W. Zhang, V. Tyberkevych, W.-K. Kwok, A. Hoffmann, V. Novosad, *J Appl Phys*. **128**, 130902 (2020).

67. F. Vanderveken, F. Ciubotaru, C. Adelmann, in *Chirality, Magnetism and Magnetoelectricity: Separate Phenomena and Joint Effects in Metamaterial Structures*, E. Kamenetskii, Ed. (Springer International Publishing, Cham, 2021), pp. 287–322.

68. T. Hioki, Y. Hashimoto, E. Saitoh, *Commun Phys*. **5**, 115 (2022).

69. A. Kamra, H. Keshtgar, P. Yan, G. E. W. Bauer, *Phys Rev B*. **91**, 104409 (2015).

70. C. Berk, M. Jaris, W. Yang, S. Dhuey, S. Cabrini, H. Schmidt, *Nat Commun*. **10**, 2652 (2019).

71. F. Godejohann, A. V Scherbakov, S. M. Kukhtaruk, A. N. Poddubny, D. D. Yaremkevich, M. Wang, A. Nadzeyka, D. R. Yakovlev, A. W. Rushforth, A. V Akimov, M. Bayer, *Phys Rev B*. **102**, 144438 (2020).

72. K. An, A. N. Litvinenko, R. Kohno, A. A. Fuad, V. V Naletov, L. Vila, U. Ebels, G. de Loubens, H. Hurdequint, N. Beaulieu, J. Ben Youssef, N. Vukadinovic, G. E. W. Bauer, A. N. Slavin, V. S. Tiberkevich, O. Klein, *Phys Rev B*. **101**, 60407 (2020).

73. J. Zhang, M. Chen, J. Chen, K. Yamamoto, H. Wang, M. Hamdi, Y. Sun, K. Wagner, W. He, Y. Zhang, J. Ma, P. Gao, X. Han, D. Yu, P. Maletinsky, J.-P. Ansermet, S. Maekawa, D. Grundler, C.-W. Nan, H. Yu, *Nat Commun*. **12**, 7258 (2021).

74. N. Ogawa, W. Koshibae, A. J. Beekman, N. Nagaosa, M. Kubota, M. Kawasaki, Y. Tokura, *PNAS* **112**, 8977–8981 (2015).

75. A. V Azovtsev, N. A. Pertsev, *Phys Rev B*. **100**, 224405 (2019).

76. C. Gonzalez-Ballestero, D. Hümmer, J. Gieseler, O. Romero-Isart, *Phys Rev B*. **101**, 125404 (2020).

77. Z.-Y. Fan, H. Qian, J. Li, *Quantum Sci Technol*. **8**, 015014 (2023).

78. J.-M. Hu, Z. Li, L.-Q. Chen, C.-W. Nan, *Nat Commun*. **2**, 553 (2011).

79. J.-M. Hu, Z. Li, J. Wang, C. W. Nan, *J Appl Phys*. **107**, 093912 (2010).

80. A. Chen, Y. Wen, B. Fang, Y. Zhao, Q. Zhang, Y. Chang, P. Li, H. Wu, H. Huang, Y. Lu, Z. Zeng, J. Cai, X. Han, T. Wu, X.-X. Zhang, Y. Zhao, *Nat Commun*. **10**, 243 (2019).

81. J.-M. Hu, T. Yang, J. Wang, H. Huang, J. Zhang, L.-Q. Chen, C.-W. Nan, *Nano Lett*. **15**, 616–622 (2015).

82. M. Ghidini, R. Pellicelli, J. L. Prieto, X. Moya, J. Soussi, J. Briscoe, S. Dunn, N. D. Mathur, *Nat Commun*. **4**, 1453 (2013).

83. J.-M. Hu, T. Yang, K. Momeni, X. Cheng, L. Chen, S. Lei, S. Zhang, S. Trolier-McKinstry, V. Gopalan, G. P. Carman, C.-W. Nan, L.-Q. Chen, *Nano Lett*. **16**, 2341–2348 (2016).

84. H. X. Wei, F. Q. Zhu, X. F. Han, Z. C. Wen, C. L. Chien, *Phys Rev B*. **77**, 224432 (2008).

85. H. Sohn, M. E. Nowakowski, C. Liang, J. L. Hockel, K. Wetzlar, S. Keller, B. M. McLellan, M. A. Marcus, A. Doran, A. Young, M. Kläui, G. P. Carman, J. Bokor, R. N. Candler, *ACS Nano*. **9**, 4814–4826 (2015).

86. J.-M. Hu, T. Yang, L.-Q. Chen, *NPJ Comput Mater*. **4**, 62 (2018).

87. J.-M. Hu, T. Yang, L.-Q. Chen, *Acta Mater*. **183**, 145–154 (2020).

88. Y. Wang, L. Wang, J. Xia, Z. Lai, G. Tian, X. Zhang, Z. Hou, X. Gao, W. Mi, C. Feng, M. Zeng, G. Zhou, G. Yu, G. Wu, Y. Zhou, W. Wang, X. Zhang, J. Liu, *Nat Commun*. **11**, 3577 (2020).

89. Y. Ba, S. Zhuang, Y. Zhang, Y. Wang, Y. Gao, H. Zhou, M. Chen, W. Sun, Q. Liu, G. Chai, J. Ma, Y. Zhang, H. Tian, H. Du, W. Jiang, C. Nan, J.-M. Hu, Y. Zhao, *Nat Commun*. **12**, 322 (2021).

90. A. V Scherbakov, T. L. Linnik, S. M. Kukhtaruk, D. R. Yakovlev, A. Nadzeyka, A. W. Rushforth, A. V Akimov, M. Bayer, *Photoacoustics*. **34**, 100565 (2023).

91. T. Henighan, M. Trigo, S. Bonetti, P. Granitzka, D. Higley, Z. Chen, M. P. Jiang, R. Kukreja, A. Gray, A. H. Reid, E. Jal, M. C. Hoffmann, M. Kozina, S. Song, M. Chollet, D. Zhu, P. F. Xu, J. Jeong, K. Carva, P. Maldonado, P. M. Oppeneer, M. G. Samant, S. S. P. Parkin, D. A. Reis, H. A. Dürr, *Phys Rev B*. **93**, 220301 (2016).

92. V. S. Vlasov, A. V Golov, L. N. Kotov, V. I. Shcheglov, A. M. Lomonosov, V. V Temnov, *Acoust Phys*. **68**, 18–47 (2022).

93. Z. Yao, R. U. Tok, T. Itoh, Y. E. Wang, *IEEE Trans Microw Theory Tech*. **66**, 2683–2696 (2018).

94. S. Couture, R. Chang, I. Volvach, A. Goncharov, V. Lomakin, *IEEE Trans Magn*. **53**, 1–9 (2017).

95. S. Zhuang, X. Zhang, Y. Zhu, N. X. Sun, C.-B. Eom, P. G. Evans, J.-M. Hu, *Physical Review Applied (Under Review)* (2024).

96. E. Saitoh, M. Ueda, H. Miyajima, G. Tatara, *Appl Phys Lett*. **88**, 182509 (2006).

97. C. Hahn, G. de Loubens, M. Viret, O. Klein, V. V Naletov, J. Ben Youssef, *Phys Rev Lett*. **111**, 217204 (2013).

98. S. Zhuang, P. B. Meisenheimer, J. Heron, J.-M. Hu, *ACS Appl Mater Interfaces*. **14**, 52575–52577 (2022).

99. Y. Tserkovnyak, A. Brataas, G. E. W. Bauer, *Phys Rev B*. **66**, 224403 (2002).

100. I. Razdolski, A. Alekhin, N. Ilin, J. P. Meyburg, V. Roddatis, D. Diesing, U. Bovensiepen, A. Melnikov, *Nat Commun*. **8**, 15007 (2017).

101. R. Salikhov, I. Ilyakov, L. Körber, A. Kákay, R. A. Gallardo, A. Ponomaryov, J.-C. Deinert, T. V. A. G. de Oliveira, K. Lenz, J. Fassbender, S. Bonetti, O. Hellwig, J. Lindner, S. Kovalev, *Nat Phys*. **19**, 529–535 (2023).

102. V. Besse, A. V Golov, V. S. Vlasov, A. Alekhin, D. Kuzmin, I. V Bychkov, L. N. Kotov, V. V Temnov, *J Magn Magn Mater*. **502**, 166320 (2020).

103. A. V Azovtsev, N. A. Pertsev, *Phys Rev Mater*. **4**, 64418 (2020).

104. U. Vernik, A. M. Lomonosov, V. S. Vlasov, L. N. Kotov, D. A. Kuzmin, I. V Bychkov, P. Vavassori, V. V Temnov, *Phys. Rev. B*. **106**, 144420 (2022).

105. D. Du, J. Hu, J. K. Kawasaki, *Appl Phys Lett*. **122**, 170501 (2023).

106. Z. LaDuca, K. Su, S. Manzo, M. S. Arnold, J. K. Kawasaki, *Phys Rev Mater*. **7**, 83401 (2023).

107. S. S. Hong, M. Gu, M. Verma, V. Harbola, B. Y. Wang, D. Lu, A. Vailionis, Y. Hikita, R. Pentcheva, J. M. Rondinelli, H. Y. Hwang, *Science* **368**, 71–76 (2020).

108. S. Jiang, H. Xie, J. Shan, K. F. Mak, *Nat Mater*. **19**, 1295–1299 (2020).

109. D. D. Sheka, *Appl Phys Lett*. **118**, 230502 (2021).

110. R. Streubel, E. Y. Tsymbal, P. Fischer, *J Appl Phys*. **129**, 210902 (2021).

111. D. Makarov, D. D. Sheka, *Curvilinear Micromagnetism: From Fundamentals to Applications* (Springer International Publishing, 2022), *Topics in Applied Physics*.

112. C. A. Potts, Y. Huang, V. A. S. V Bittencourt, S. Viola Kusminskiy, J. P. Davis, *Phys Rev B*. **107**, L140405 (2023).

113. V. A. S. V Bittencourt, C. A. Potts, Y. Huang, J. P. Davis, S. Viola Kusminskiy, *Phys Rev B*. **107**, 144411 (2023).

114. D. Lachance-Quirion, Y. Tabuchi, A. Gloppe, K. Usami, Y. Nakamura, *Applied Physics Express*. **12**, 70101 (2019).

115. N. Lauk, N. Sinclair, S. Barzanjeh, J. P. Covey, M. Saffman, M. Spiropulu, C. Simon, *Quantum Sci Technol*. **5**, 020501 (2020).

116. D. Montes de Oca Zapiain, J. A. Stewart, R. Dingreville, *NPJ Comput Mater*. **7**, 3 (2021).

117. W. Li, M. Z. Bazant, J. Zhu, *Comput Methods Appl Mech Eng*. **416**, 116299 (2023).

118. M. Dai, M. F. Demirel, Y. Liang, J.-M. Hu, *NPJ Comput Mater*. **7**, 103 (2021).

119. K. Alhada-Lahbabi, D. Deleruyelle, B. Gautier, *ACS Appl Electron Mater*. **5**, 3894–3907 (2023).

120. M. Dai, M. F. Demirel, X. Liu, Y. Liang, J.-M. Hu, *Comput Mater Sci*. **230**, 112461 (2023).

Authors Contributions

J.-M.H. conceptualized, designed, and wrote this review article. J.-M.H. also performed the literature search and data analysis.

Acknowledgements and Funding Information

The author acknowledges support from the National Science Foundation (NSF) under the grant number DMR-2237884. Partial support for manuscript preparation was provided by the Wisconsin MRSEC (DMR-2309000). The examples of magnetomechanical devices presented in this paper benefit from the insights and collaborative efforts from all the co-authors of the relevant papers cited, including Z. Li, L.-Q. Chen, C.-W. Nan, T. Yang, J. Wang, H. Huang, J. Zhang, K. Momeni, X. Cheng, L. Chen, S. Lei, S. Zhang, S. Trolier-McKinstry, V. Gopalan, G.P. Carman, S. Zhuang, P.B. Meisenheimer, J. Heron, X. Zhang, Y. Zhu, N.X. Sun, C.-B. Eom, and P.G. Evans. The author also thanks S. Zhuang for assistance in the analytical calculation shown in Figure 2. Fruitful discussions with Changchun Zhong, Wei Zhang, Jun Xiao, and Jason Kawasaki are greatly appreciated.